Microscopic description of the evolution of the local structure and an evaluation of the chemical pressure concept in a solid solution

Soham Mukherjee,[1] Angshuman Nag,[1] Vancho Kocevski,[2] Pralay K. Santra,[1] Mahalingam Balasubramanian,[3] Soma Chattopadhyay,[4,5] Tomohiro Shibata,[4,5] Franz Schaefers,[6] Jan Rusz,[2] Celine Gerard,[2,*] Olle Eriksson,[2] C. U. Segre,[5] and D. D. Sarma[1,2,7,†]

[1]*Solid State and Structural Chemistry Unit, Indian Institute of Science, Bangalore 560012, India*
[2]*Division of Materials Theory, Department of Physics and Astronomy, Uppsala University, Box 516, SE-751 20 Uppsala, Sweden*
[3]*X-ray Science Division, Argonne National Laboratory, Argonne, Illinois 60439, USA*
[4]*MRCAT, Sector 10, Bldg. 433B, Argonne National Laboratory, Argonne, Illinois 60439, USA*
[5]*CSRRI & Department of Physics, Illinois Institute of Technology, Chicago, Illinois 60616, USA*
[6]*Institute for Nanometre Optics and Technology, HZB-BESSY II, Albert-Einstein-Strasse 15, D-12489 Berlin, Germany*
[7]*Council of Scientific and Industrial Research—Network of Institutes for Solar Energy (CSIR—NISE), New Delhi, India*

(Received 10 October 2013; revised manuscript received 28 May 2014; published 26 June 2014)

Extended x-ray absorption fine-structure studies have been performed at the Zn K and Cd K edges for a series of solid solutions of wurtzite $Zn_{1-x}Cd_xS$ samples with $x = 0.0$, 0.1, 0.25, 0.5, 0.75, and 1.0, where the lattice parameter as a function of x evolves according to the well-known Vegard's law. In conjunction with extensive, large-scale first-principles electronic structure calculations with full geometry optimizations, these results establish that the percentage variation in the nearest-neighbor bond distances are lower by nearly an order of magnitude compared to what would be expected on the basis of lattice parameter variation, seriously undermining the chemical pressure concept. With experimental results that allow us to probe up to the third coordination shell distances, we provide a direct description of how the local structure, apparently inconsistent with the global structure, evolves very rapidly with interatomic distances to become consistent with it. We show that the basic features of this structural evolution with the composition can be visualized with nearly invariant Zn-S_4 and Cd-S_4 tetrahedral units retaining their structural integrity, while the tilts between these tetrahedral building blocks change with composition to conform to the changing lattice parameters according to the Vegard's law within a relatively short length scale. These results underline the limits of applicability of the chemical pressure concept that has been a favored tool of experimentalists to control physical properties of a large variety of condensed matter systems.

DOI: 10.1103/PhysRevB.89.224105 PACS number(s): 61.05.cj, 61.66.Dk, 78.70.Dm

I. INTRODUCTION

X-ray diffraction (XRD) is the standard tool used to investigate structural parameters of all crystalline samples, specifically those of crystalline alloys. Many such studies on a diverse range of alloys have established that lattice parameters vary smoothly, and most often almost linearly [1–8], with composition between the lattice parameters of the end-members of the alloy composition. This is well-known as Vegard's law [9,10], which has been used extensively to determine the stoichiometry [11–13] of different systems, though there are also examples of either positive or negative deviations [14–22] from Vegard's law. Several theoretical models [23–27] have been developed in order to understand the nature of alloying and to predict their tendency to deviate from Vegard's law. However, in situations where the lattice parameters of the pure end components differ by less than 5%, the evolution of lattice parameters as a function of the composition is found to be described very well by Vegard's law [28]. At the simplest level of theoretical descriptions, a random occurrence of two different atoms at a given crystallographic site for an alloy is represented by a virtual atom whose potential is assumed to be given by the composition averaged potentials of the two distinct atoms, thereby smoothly interpolating physical properties, including lattice parameters, of the solid solution between the corresponding properties of the end members. Thus, the explanation for the experimentally observed Vegard's law for lattice parameters is easily understood within this approximation, known as the virtual crystal approximation (VCA).

An associated concept, termed as "chemical pressure" [29–33], has long been used in tuning properties of a given system by introducing atoms that are larger or smaller than the ones being substituted in the system. Extending the observation of a smooth interpolation of the lattice parameters between the limiting end compounds, e.g., AC and BC in $A_{1-x}B_xC$ alloy, to the A-C and B-C bond lengths, as would be suggested on the basis of VCA calculations, such a substitution of A with B having a different size is expected to smoothly change the A-C bond length proportional to the change in the lattice parameter. If the size of atom B is smaller than that of A, one expects a contraction of the A-C bond on progressive introduction of B into the system, just as would happen for AC under an applied external pressure. Thus, such chemical substitutions have been used extensively for generating internally a pressure equivalent effect, known as the chemical pressure. It has not only been used for facile control of pressure effects chemically,

*Present address: Pprime Inst, Phys & Mech Mat Dept, CNRS UPR 3346, Univ Poitiers, ISAE ENSMA, F-86961 Futuroscope, Chasseneuil, France.
†Also at Jawaharlal Nehru Centre for Advanced Scientific Research; sarma@sscu.iisc.ernet.in

it also provides the possibility of exerting negative (tensile) "pressure" on the sample by doping a larger sized atom for a smaller one; such a negative pressure would otherwise be inaccessible, establishing the power and explaining the popularity of this technique.

Going beyond such a broad stroke description of global changes in the lattice parameters, probed by XRD, it is evident that such an approach as embodied in Vegard's law or the VCA cannot be true at a microscopic level. For example, it is highly improbable for *A*-*C* and *B*-*C* bond lengths to adopt a single average value in the spirit of the VCA, this average bond-length then varying linearly with the composition of $A_{1-x}B_xC$ alloy. Microscopic, local structural information obtained by extended x-ray absorption fine-structure studies (EXAFS) of several alloys have indeed established beyond doubt that the first near-neighbor bond lengths [2–4,34–55], *A*-*C* and *B*-*C*, remain close to their values in the corresponding end-members instead of adopting a single average value. In a few reports, such analyses were extended up to the higher coordination shells [4,43–49] to check if such discrepancies exist at longer interatomic distances. Distortions induced in a system due to doping not only affects the interatomic distances but also the angles contained by them, which tend to buckle accordingly [2,50–55], deviating from their ideal bond angle values. Theoretical models [3,56] have also been developed for the local structure of such disordered alloys. Clearly, the observation of the validity of Vegard's law for the global structure from XRD in all such cases must be interpreted within the aforementioned constraints of experimental observations of relative invariance of the individual bond lengths of the constituents. It should be noted that the validity of Vegard's law can be rationalized in terms of a large length-scale view of the lattice even in absence of any variation in the individual bond lengths since the pair distribution function will statistically average the two separate, component bond lengths at larger distances.

It is clear from the above discussion that it is important to carry out EXAFS investigations of a suitable alloy system so that the data can be collected over a wide range of k values with very good signal-to-noise ratios. This would allow one to critically evaluate the evolution of the local structure to the global one by extending the range of interatomic distances as well as allow one to address the concept of the chemical pressure, attempting to simulate consequences of the application of a physical pressure on the sample by doping atoms of a dissimilar size into the sample. In order to achieve this goal, we chose ternary alloy system $Zn_{1-x}Cd_xS$, which forms a complete series of solid solutions across the composition range. $Zn_{1-x}Cd_xS$ also has interesting material properties that have recently been investigated quite extensively due to their wide range of applicability in photocatalysis [57,58], as tunable photoluminescence emission materials [59–63], as nonvolatile memory devices [64], or as heterojunctions in solar cells [65,66]. The presence of Zn and Cd with largely different scattering properties makes this solid solution a suitable candidate for the purpose of our study. This series of compounds exhibits a linear lattice constant variation as a function of the composition, obeying Vegard's law. Zn^{2+} and Cd^{2+} ions have considerably different ionic sizes, reflected in the large changes in the lattice parameters of the pure compounds, ZnS and CdS. The most important aspect relevant to the present study is the fact that the alloy forms with random substitutions at the cation site, in spite of the large size difference between Zn and Cd, without any evidence for local clustering of Zn or Cd ions, as established by our investigation described later. With the solid solution forming right across the composition range, it also allows us to study the compressive chemical pressure at the Cd-rich end and the tensile chemical "pressure" in the Zn-rich end of the composition. We obtained high quality EXAFS data for $x = 0.0, 0.1, 0.25, 0.5, 0.75$, and 1.0 in a $Zn_{1-x}Cd_xS$ series over a wide range of k values and at a low temperature of 25 K, enabling us to analyze up to the third coordination shells for both Zn and Cd, extending the real space local information to a large enough distance that allows us to follow the evolution of the local structure into the global structure with an increasing length scale of the distance probed. It also allows us to discuss the concept of the "chemical pressure" and its limitations from a microscopic description of the structure. We present detailed first-principles calculations on the same series of compounds with full geometry optimization to validate the microscopic structural models obtained from EXAFS and to obtain further insight into these issues that are beyond the sensitivity of the experimental techniques.

II. COMPUTATIONAL, DATA REDUCTION AND EXPERIMENTAL DETAILS

We synthesized the series of $Zn_{1-x}Cd_xS$ ternary alloys, with x values equal to 0.0, 0.1, 0.25, 0.5, 0.75, and 1.0. Stoichiometric amounts of ZnS and CdS were ground thoroughly together to ensure a homogenous mixture, pelletized, and followed by heating at 750 °C in evacuated quartz tubes under high vacuum conditions ($<10^{-6}$ mbar) to avoid any oxidation. For undoped ZnS, the zinc-blende structure is the thermodynamically most stable form, but it can be converted to the wurtzite phase by annealing at 1020 °C under ambient pressure [67]. Powder XRD measurements were performed with the help of Siemens and Philips diffractometers for determination of crystallographic phase purity of samples. The XRD patterns reported in this paper were collected with Cu K_α radiation at room temperature. A slower scan speed was used to improve the signal-to-noise ratio in order to ascertain the absence of any impurity phases. Energy dispersive analyses of x rays (EDAX) were carried out for each sample to estimate the chemical composition as well as the degree of chemical homogeneity present in various spots within the sample using a JEOL-JSM-5600LV high resolution scanning electron microscope.

In order to study the local structure around the component ions in the system, we performed room temperature (300 K) EXAFS measurements at the Zn K edge for wurtzite $Zn_{1-x}Cd_xS$ samples at the KMC-2 beamline of the BESSY-II storage ring in Berlin. We also have low temperature data (25 K) for the samples ($x = 0.0, 0.25, 0.5, 0.75$, and 1.0) collected at both Zn K and Cd K edges in transmission mode from the experiments performed at the Sector 20 bending magnet beamline at the Advanced Photon Source, Argonne National Laboratory, Chicago. Both Zn and Cd foils were measured as the reference channel to check for any inconsistency in the energy shifts during the data collection at the respective elemental edges. We performed multiple scans

for all the data sets, which were properly aligned, merged, and processed using the program Athena [68]. Going down to such low temperatures (25 K) largely suppresses the thermal disorder within the systems, which allows us to extract sharp, distinguishable features in the $\chi(k)$ function up to very high photoelectron wave numbers ($k \sim 15.0$ Å^{-1}). Detailed fits to the data were carried out up to the maximum k range of 14.0 Å^{-1} using the standard EXAFS equation with the help of the Artemis program [68], which uses FEFF 6.0 code [69] to calculate the scattering amplitudes and phases for all possible scattering events. The $S_0{}^2$ values, for Zn (0.91) and Cd (0.78) edges, obtained from fits to the end members were retained as constant values during simultaneous fits to Zn K and Cd K edges for each composition. The fits to the end members ZnS ($x = 0.0$) and CdS ($x = 1.0$) in both real parts of the Fourier transform (Re[$\chi(R)$]) and the Fourier filtered k data (Re[$\chi(q)$]) are presented in Supplemental Material Fig. S1 [70]. The corresponding simultaneous fits to Zn and Cd data for the intermediate compositions ($x = 0.25$, 0.50, and 0.75) are presented in Supplemental Material Fig. S2 [70]. All the fits were performed over the identical k-range (2.7–14.0 Å^{-1}) using a Hanning window over the same R range (1.35–4.5 Å). Necessary restrictions were incorporated into the fitting model on the basis of the knowledge of the crystal structure and to estimate the edge shift (δE_0), bond distances (R), bond angles (θ_{M-S-M}), coordination number (N) for the mixed cation sublattice, and the pseudo-Debye-Waller factors (σ^2). For the first coordination shell, we find that the degeneracy in all our analyses is always close to 4, as expected for the wurtzite phase. Similarly, an independent estimation of the coordination number for the second nearest neighbor yields values close to 12 for all of the systems, following the crystallographic information. Thus, the analyses were carried out by fixing the first and second nearest-neighbor coordination numbers to 4 and 12, respectively, to lower the number of variables and estimate the local parameters for all subsequent analyses. Since all samples in the present study have a wurtzite phase, we calculated EXAFS patterns for hexagonal ZnS and CdS according to the available crystal structure information (Inorganic Crystal Structure Database [ICSD] 67453 and ICSD 154186) as the starting model to fit the nearest neighbors. The difference between the longer M-S ($M =$ Zn or Cd) bond distance and the shorter one in this crystal structure was much smaller than the experimental EXAFS resolution; therefore, these bond distances were modeled as a single distance with degeneracy 4, as shown in Supplemental Material Table S1 [70]. Similarly, for the second nearest neighbors, one can essentially model the two different M-M distances as a single distance with degeneracy 12. However, for the third near-neighbor shell, the situation is slightly different for a wurtzite system. Neglecting contributions from multiple scattering paths, the FEFF calculation shows that there exists a total of 10 M-S ($M =$ Zn or Cd) atomic pair correlations (single scattering events) in three sets [1 + 3 + 6] for a hexagonal phase (Supplemental Material Fig. S3 [70]) that contribute to the EXAFS data. Thus, there are three M-S bond lengths characterizing the third coordination shell for the wurtzite structure. For example, Zn-S distances in the third coordination shell for pure ZnS are 3.8339 Å, 4.4585 Å, and 4.5038 Å, with 1, 3, and 6 as the coordination numbers. The corresponding numbers for Cd-S distances in pure CdS are 4.1841 Å, 4.8473 Å, and 4.8499 Å. Analyses of our EXAFS data for the third shell of ZnS and CdS are in good agreement with these crystallographic data, establishing the high data quality in the present case. However, for intermediate compositions, we expect a range of interatomic distances around three such average distances of M-S distances depending on the exact number of Zn and Cd in the intervening second shell. This makes it impossible to distinguish between the two long M-S distances. Therefore, we have analyzed the M-S third shell distances in terms of only two bond lengths, one short (M-S1) and one long (M-S2) with coordination numbers of 1 and 9, respectively. It is also obvious that the short bond with only one such distance among a total of 10 M-S distances in the third shell will necessarily be less accurately determined due to its overall lower contribution to the total EXAFS. We note here that even if the disorder existing in our systems is mostly static in origin, we still expect a large σ^2 for the third near-neighbor environment, owing to its broad distribution of M-S distances within the provided shell volume. This results in partial filtering of the M-S1 and M-S2 contributions into the second shell correlations, which prompted us to model the significantly broad features beyond ~2.8 Å using a combination of the scattering atoms present in the second and third nearest coordination shells.

To provide a theoretical validation of the microscopic structural information extracted from experimental EXAFS data, we carried out extensive first-principles calculations for a large number of alloyed compositions of ZnS and CdS. For this purpose we chose different x values in $Zn_{1-x}Cd_xS$ compositions: $x = 0.0$, 0.25, 0.5, 0.75, and 1.0. We consider a supercell containing 288 atoms. To make the three different alloy ($0 < x < 1$) compositions, one cation type is randomly substituted with the other cation type. For each alloy composition, three different realizations of random structures were considered and averaged. In other words, we carried out nine supercell calculations, three for each alloy composition $x = 0.25$, 0.5, and 0.75.

These calculations were performed using the local density approximation (LDA) exchange-correlation potential with the SIESTA pseudopotential package [71] and Ceperley-Alder parameterization of the exchange-correlation functional [72]. A double zeta polarization (DZP) basis for the three types of atoms was used. The atom positions were relaxed until the forces acting on every atom were lower than 0.04 eV/Å. During the relaxation, the volume of the cells was allowed to change. At the beginning, only the gamma point was used for relaxing the structure. To verify that the relaxed structures are large enough, a single randomly chosen calculation was reconverged using 105 k-points. The forces were found to be converged within 0.043 eV/Å, indicating that our models are large enough to be treated just with 1 k-point.

III. RESULTS AND DISCUSSION

X-ray diffraction data for $Zn_{1-x}Cd_xS$ alloys (not shown) reveal that all the alloyed samples exhibit wurtzite structure with no signature of any impurity phase. From experiment and first-principles calculations, we calculated the lattice parameters as well as the interplanar spacings for all the samples. The lattice parameters obtained from experiment and theory

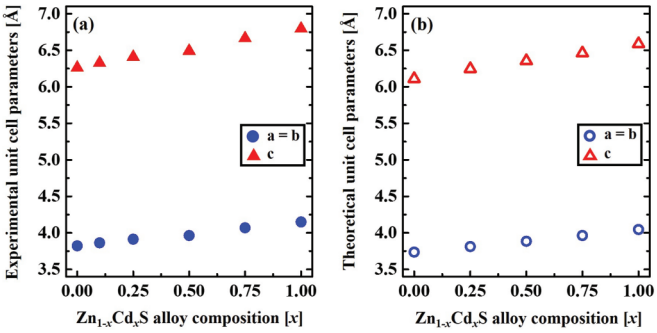

FIG. 1. (Color online) Linear variation of lattice parameters for $Zn_{1-x}Cd_xS$ alloys as a function of composition obtained from (a) experiment and (b) theory. Unit cell parameters a/b and c are represented as solid blue circles and solid red up-triangles, respectively; the theoretical values obtained from geometry optimization procedure are shown with corresponding open symbols. A comparison of the panels (a) and (b) shows the underestimation of values obtained from calculations compared to the experimental data points, but the important point to notice here is that their trends are very similar, as obtained from the slope of lines joining the individual data points.

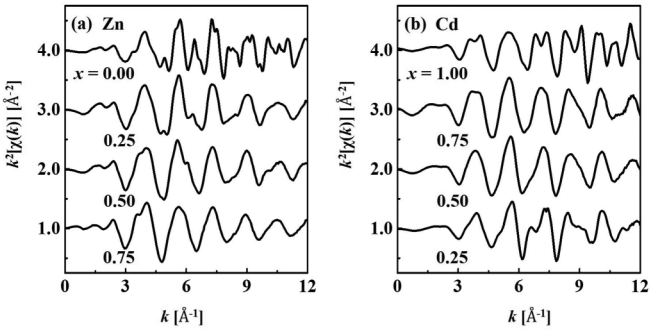

FIG. 2. k^2-weighted $\chi(k)$ oscillations for (a) Zn K edge and (b) Cd K edge for $Zn_{1-x}Cd_xS$ solid solution series. All the data sets were collected at 25 K. The plots are presented with a constant offset of 1.0 units for the purpose of better viewing.

are plotted together in Figs. 1(a) and 1(b), which shows an essentially linear variation with the composition. As expected, with an increasing substitution of larger Cd^{2+} ions (0.92 Å) with smaller Zn^{2+} ions (0.74 Å), the cell parameters gradually decrease as a consequence of lower interplanar distances. The agreement between the experimental and theoretical results is very good, with a slight systematic underestimation from the theory, which is a known artifact of the used exchange correlation potential, LDA [73,74]. The interplanar spacings and the cell parameters for alloys are calculated from the XRD peak positions for the corresponding alloys using Bragg's law. XRD allows one to estimate the composition, x, in the alloy system, $Zn_{1-x}Cd_xS$, by resolving the interplanar spacing of the alloy ($d_{(Zn_{1-x}Cd_x)S}$) into a linear combination of the interplanar spacings of the constituent end member systems, ZnS and CdS (Eq. 1), following Vegard's law. The [101] lattice plane has been used as a representative in Eq. 1:

$$d_{(Zn_{1-x}Cd_x)S}[101] = (1-x) * d_{ZnS}[101] + (x) * d_{CdS}[101]. \quad (1)$$

Another independent experimental estimate of the composition, x, was obtained from EDAX measurements for all samples of the $Zn_{1-x}Cd_xS$ series. We find that the compositions estimated from diffraction data and those from EDAX both closely resemble the starting compositions in the synthesis of the alloy within a maximum spread $<\pm 7\%$, confirming a high degree of chemical homogeneity for these samples and a remarkable adherence to Vegard's law right across the composition range.

From our XAFS measurements at the Zn K and Cd K edges, we find that the position and shape of both elemental edges (not shown) remain almost identical, regardless of the alloy composition, thus indicating similar oxidation state and crystal environments for all the samples, which in our case are Zn^{2+} and Cd^{2+} ions tetrahedrally coordinated by 4 S^{2-} ions. The k-space EXAFS data sets obtained at the Zn K and Cd K edges at the low temperature in the transmission mode for all samples of the $Zn_{1-x}Cd_xS$ series are shown in Fig. 2. The k-space oscillations show striking similarities in the major frequency components for the same edge across the entire solid solution series, suggesting very similar environments around each type of cations, namely Zn and Cd, in all these samples. The corresponding Fourier transforms (R space) for all the data sets are shown in Fig. 3. As evident from Fig. 3, the real-space data show that the first peak in every case is sharp and quite similar to each other, whereas the second peak shows distinct changes with a significant broadening for the intermediate or alloyed compositions, arising mostly due to interference. This behavior can be readily understood by noting the fact that the first coordination shell for each cation is invariably S, independent of the composition, whereas the second neighbor shell of a cation is a random mixture of the two types of cations (Zn and Cd) depending on the composition of the alloyed sample. While the first shell features hint at similar environments for a particular absorber across the entire range of the solid solution series, the higher shell features are rather broad due to interference. So for the higher shells, in addition to the Gaussian distribution to the interatomic distances, we included an asymmetry broadening parameter to account for the peak widths. However, we find that the contribution from

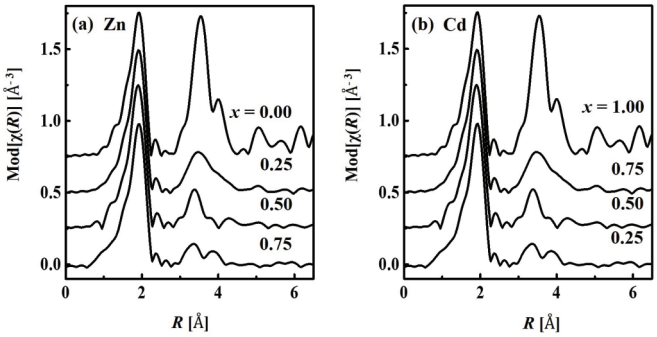

FIG. 3. Magnitude of the Fourier transform of experimental EXAFS functions ($k^2 \times \chi(R)$) for (a) Zn K edge and (b) Cd K edge for $Zn_{1-x}Cd_xS$ solid solution series. All the data sets were collected at 25 K. The plots are presented with a constant offset of 0.25 units for the purpose of better viewing.

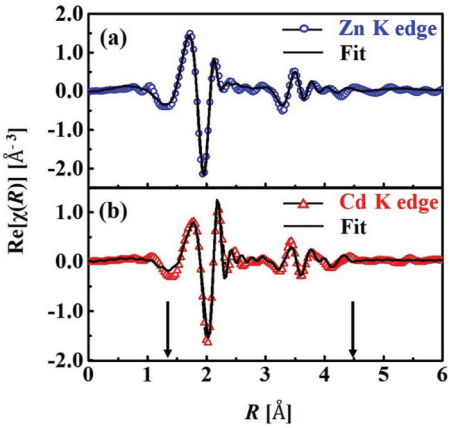

FIG. 4. (Color online) The real component of the R-space data and the corresponding fits to the (a) Zn K edge (blue open circles) and (b) the Cd K edge (red open up-triangles) for $Zn_{0.5}Cd_{0.5}S$ system, a representative of the $Zn_{1-x}Cd_xS$ solid solution series. The fit range (1.35–4.5 Å) in R space is marked by black vertical arrows.

asymmetric broadening is extremely low and hence ignored in the final fitting models.

We have analyzed the low temperature (25 K) Zn K and Cd K edge EXAFS of three alloys together with the two end members to determine the change in the Zn-S and Cd-S bond lengths in the first shell, Zn-Zn, Zn-Cd, and Cd-Cd distances in the second shell and a farther away S in the third shell from the absorber atom (Zn or Cd) as a function of the alloy composition. The real components of the R-space data and the corresponding fits for a representative case, chosen as the $Zn_{0.5}Cd_{0.5}S$ compound, are shown in Fig. 4.

A. First shell environment

First shell (nearest-neighbor) fits to the EXAFS data have been performed for all samples on both Zn K and Cd K edges as a function of the composition. The details of the local parameters for the first coordination shell are presented in Supplemental Material Table S1 [70]. The Zn-S and Cd-S bond distances, extracted from EXAFS fitting and from geometry optimizations within first-principle calculations, are plotted in Fig. 5 as a function of the composition. Clearly the component bond distances for both Zn-S and Cd-S roughly retain the original bond length of the parent end members of the series. This is similar to results previously reported for other systems [2–4,34–55] with different structure types. This is in complete contrast to the simplistic expectation based on VCA or by transferring the observed linear variation of the lattice parameter in agreement with Vegard's law to bond lengths that motivates the concept of the chemical pressure. A closer look reveals a slight increase of the Zn-S bond length with an increasing Cd incorporation, suggesting that the Zn-S_4 tetrahedra tend to dilate due to the Cd substitution. On the other hand, the Cd-S_4 tetrahedra shrink with increasing Zn concentration, as shown by the variation of the Cd-S bond length in Fig. 5. This is exactly what would be expected on the basis of the chemical pressure concept, with the substitution of the larger Cd^{2+} ion for the smaller Zn^{2+} ion providing a tensile strain, dilating the Zn-S_4 tetrahedra, while

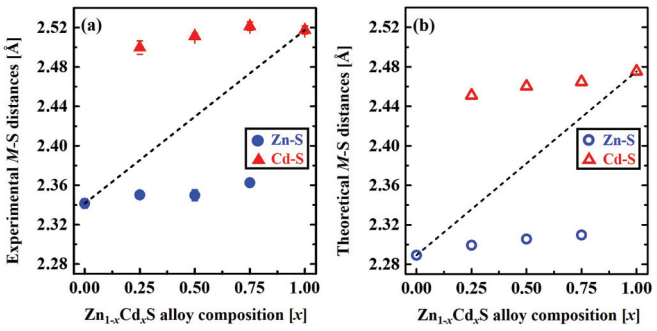

FIG. 5. (Color online) First shell bond distances for $Zn_{1-x}Cd_xS$ alloys obtained from (a) experiment and (b) theory. The experimental results are shown with solid blue circles for Zn-S and solid red up-triangles for Cd-S, whereas the theoretical values obtained from geometry optimization procedure are shown with corresponding open symbols. The black dashed line connecting the M-S (M = Zn or Cd) bond lengths of the pure end compounds schematically shows the nature of a hypothetical average M-S bond length across the series for both experiment and theory. Error limits for the theoretical data points, being smaller than the symbol size, has been removed. A comparison of (a) and (b) shows the underestimation of values obtained from calculations compared to the experimental data points, but the important point to notice here is that their trends are very similar, as obtained from the slope of lines joining the individual data points.

the reverse substitution of smaller Zn^{2+} for larger Cd^{2+} leads to a compressive strain of the Cd-S_4 tetrahedra, apparently validating the chemical pressure concept. However, even at the level of the first coordination shell, it is clear that in terms of quantitative expectations, the chemical pressure effect falls far short of what would be expected on the basis of the variation in the lattice parameters, or in other words, according to the dashed line in Fig. 5. In order to quantify the deviation of the obtained changes in the bond distance as a function of doping from the average behavior defined by the dashed line, we first note that the bond length variation is approximately linear with the alloy composition. The slope ($m_{\text{expt.}}$) of this linear behavior defines the actual change in the bond length per unit change in composition. Thus, we can define the percentage deviation, η, as $(m_{\text{VCA}} - m_{\text{expt.}})/m_{\text{VCA}} \times 100$, where m_{VCA} denotes the slope of the dashed line. We find that the experimentally determined Zn-S and Cd-S first coordination shell bond lengths change at a much slower rate with the composition than is suggested by the dashed line with the aforesaid percentage deviation (η) for the first shell Zn-S and Cd-S bonds being as high as (89 ± 4)% and (87 ± 5)%, respectively. In order to relate our results to the concept of the chemical pressure, we calculate the chemical pressure for the 10% Cd-doped ZnS system with respect to ZnS from its bulk modulus and lattice parameters of both the systems. We find that a volume expansion of 2.029 $Å^3$ for the unit cell of ZnS due to 10% Cd doping at the Zn site (tensile stress) would translate into a "negative" chemical pressure of 2.03 GPa. Had the bond distances within the system scaled exactly with the lattice parameters following the chemical pressure concept, we would expect the corresponding Zn-S distance to increase by 0.0185 Å, whereas it changes by only 0.002 Å, which is only

about 10.8% of the expected value, seriously undermining the chemical pressure concept. This apparent discrepancy between the nearest-neighbor bond length changes, and variations in lattice parameters are addressed in detail in the next subsection, where we discuss the case of the next-nearest-neighbor distances.

We note here that the experimental M-S distances for each composition are obtained under the assumption of a single Zn-S and a single Cd-S bond length in the systems, as also in all previous EXAFS analysis of alloyed systems. However, our detailed first-principles calculations allow us to critically evaluate the validity of this universal assumption. While the calculated average Zn-S and Cd-S bond distances follow the experimentally derived values quite closely, as already discussed and shown in Fig. 5, our calculated results show a distribution of M-S bond lengths, which systematically depend on the nature of the next-near-neighbor cation. Specifically, both Zn-S and Cd-S bond lengths increase with an increasing number of Cd in the next-nearest-neighbor positions in any given alloy composition. This can be understood qualitatively in terms of the smaller ionic radius of the Zn^{2+} compared to that of Cd^{2+}. Thus, having larger number of smaller sized ions, namely Zn^{2+}, at the next-nearest-neighbor sites allow the central cationic site, independent of it being Zn or Cd, more available space and, consequently, a longer bond length. Exactly the opposite trend is observed for an increasing number of Cd^{2+} ions in the next-near-neighbor positions. These results signify that the chemical pressure is not only much less than what would be anticipated on the basis of the lattice parameter variations but also necessarily inhomogeneous, in qualitative contrast with the physical pressure. Interestingly, however, calculated results show that the maximum spread of Zn-S and Cd-S bond distances are only 0.035 Å and 0.023 Å, respectively. This is consistent with the small values of the Debye-Waller factor (σ^2) we observe for both Zn-S and Cd-S atom-pair correlations. The σ^2 values, dominated by the static component, remain more or less constant throughout the series, which shows a remarkably narrow distribution of bond distances for the first near-neighbor environment, regardless of the alloy composition. Such low variance (σ) in the Zn-S and Cd-S distances agrees well with the slight monotonic increase of Zn-S and Cd-S bond distances with increasing Cd content across the solid solution series.

B. Second shell environment

For any system in the wurtzite phase, one expects 12 atoms in the next-nearest-neighbor positions. Thus, in an alloy of the type $Zn_{1-x}Cd_xS$, a Zn atom should see a total of 12 atoms, consisting of both Zn and Cd, and their respective numbers should be determined by the stoichiometry. Any departure from this estimated number would signify a clustering [75] of some sort, for example, a composition fluctuation over a short enough length scale in the systems below the level of detection by diffraction experiments. Thus, results of the higher shell analyses can be used very effectively to qualitatively characterize the degree of randomness in such solid solutions. The second shell coordination numbers obtained from EXAFS analysis are shown in Fig. 6 in terms of the number (n_{Zn-Zn}) of Zn atoms around a Zn site and the number of (n_{Cd-Cd})

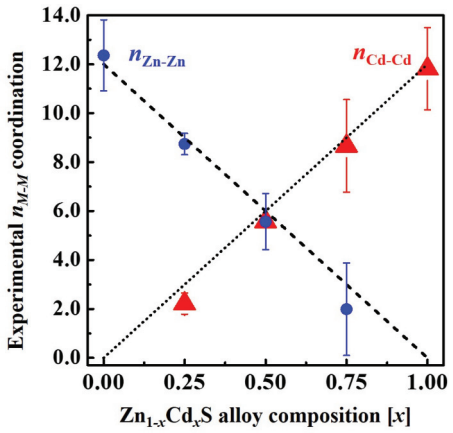

FIG. 6. (Color online) Quantitative estimate of degree of randomness in $Zn_{1-x}Cd_xS$ alloys; the number of (n_{Zn-Zn}) Zn atoms about each Zn absorber is shown in solid blue circles, and the number of (n_{Cd-Cd}) Cd atoms about each Cd absorber is shown in solid red up-triangles. The nominal composition lines for n_{Zn-Zn} and n_{Cd-Cd}, as commonly represented as n_{M-M}, are shown in black dashed and dotted lines, respectively, and comparison shows signature of random alloying.

of Cd atoms around a Cd site, evaluated from independent experiments at the Zn K edge and Cd K edge, respectively. The list of local parameters for the second near neighbors are presented in Supplemental Material Table S2 [70]. We note that this analysis was carried out by fixing the total coordination number of next nearest neighbor at 12, as mentioned previously in the Experimental Details section.

Thus, the number (n_{Cd-Zn}) of Zn sites around Cd and the number (n_{Zn-Cd}) of Cd sites around Zn are trivially related as $n_{Cd-Zn} = 12 - n_{Cd-Cd}$ and $n_{Zn-Cd} = 12 - n_{Zn-Zn}$. In the case of a perfectly random alloy, these numbers, n_{Zn-Zn} and n_{Cd-Cd}, are given directly by the composition of the alloy and are shown by the dashed line (for n_{Zn-Zn}) and the dotted line (for n_{Cd-Cd}) in Fig. 6. The estimates of n_{Zn-Zn} and n_{Cd-Cd} from experimental data are found to be in good agreement with these lines, indicating that the alloyed compositions investigated here indeed represent a random arrangement of Zn and Cd sites without any evidence of a significant clustering as compositional inhomogeneities. We note here that the bond distances and Debye-Waller factors for Zn-Cd and Cd-Zn atomic pairs, being essentially the same, were modeled as a single parameter for all the intermediate alloy compositions.

In the second shell, we need to deal with three distinct bond distances arising from a combination of Zn-Zn, Zn-Cd, and Cd-Cd distances. In the analysis of the second shell, we performed simultaneous fits at the Zn K and Cd K edges for each alloy composition, using constraints in the model based on very generic and robust crystallographic information. First of all, for any $Zn_{1-x}Cd_xS$ alloy, the concentration of Cd and Zn must add up to unity in order to maintain the charge neutrality. Second, we need to have a constraint on the number of metal "bonds" at each edge. Thus, looking at the Zn K edge for an overall wurtzite structure with a tetrahedral environment around each site, the total number of Zn and Cd ions appearing in the second shell of a Zn or Cd ion is 12. In the volume where

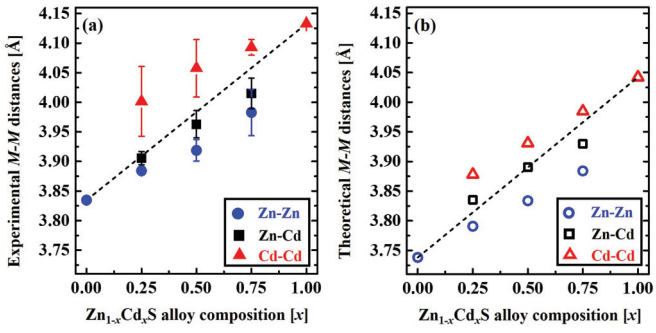

FIG. 7. (Color online) Second coordination shell interatomic distances for $Zn_{1-x}Cd_xS$ alloys obtained from (a) experiment and (b) theory. Zn-Zn (solid blue circles), Zn-Cd (solid black squares), and Cd-Cd (solid red up-triangles) interatomic distances in the second shell for $Zn_{1-x}Cd_xS$ alloys extracted from EXAFS; the theoretically calculated values from geometry optimization procedure are shown with corresponding open symbols. The black dashed line connecting the *M*-*M* (M = Zn or Cd or both) bond lengths of the pure end compounds schematically shows the nature of a hypothetical average *M*-*M* bond length across the series for both experiment and theory. Error limits for the theoretical data points, being smaller than the symbol size, have been removed. A comparison of (a) and (b) shows the underestimation of values obtained from calculations compared to the experimental data points, but the important point to notice here is that their trends are very similar, as obtained from the slope of lines joining the individual data points.

a fixed number of metal atoms are illuminated, we see a total number of metal-metal bonds in the EXAFS, either viewed from a Zn absorber or a Cd absorber. Hence the ratio of the total number of Cd-Zn bonds as viewed from the Cd atom to the total number of Zn-Cd bonds viewed from the Zn atom should be equal to the ratio of the Zn content to Cd content, as dictated by stoichiometry. In Fig. 7(a), we have plotted these three interatomic distances extracted from EXAFS results for different compositions. We have also shown the average bond distances obtained for these three bonds from theoretically obtained, geometry optimized results with corresponding open symbols in Fig. 7(b), showing the same trend as and a good agreement with the experimentally determined bond distances. The dashed line in the plot represents the variation of the hypothetical single, average bond distance with the alloy composition, as would be described within a VCA-type approach. Interestingly, in contrast to the first near-neighbor distances, we find that the second nearest-neighbor distances more closely approximate the average distance (dashed line) anticipated on the basis of the lattice parameter variation in agreement with Vegard's law. We stress here that there are still clearly observed differences between the actual bond distances obtained here at the microscopic level from EXAFS analysis compared to those expected on the basis of a single, composition weighted average value consistent with a long length-scale (global) description from XRD data for the intermediate compositions. Thus, the bond lengths for even the second coordination shell do not evolve with the composition in the expected manner, though the discrepancy clearly decreases compared to those for the first coordination shell (see Fig. 5). Expressing these deviations in the rate of change of bond lengths with the composition in terms of corresponding ηs defined earlier, we find η to be $(40 \pm 5)\%$, $(31 \pm 2)\%$, and $(46 \pm 4)\%$ for d_{Zn-Zn}, d_{Zn-Cd}, and d_{Cd-Cd}, respectively. These results show how the mismatch between the local and the global descriptions of bond distances is rapidly compensated for by the specific atomic arrangements in the alloy with an increasing length scale, resolving the apparent contradiction between the local description based on the EXAFS analysis and the global description based on the diffraction analysis. The route to this resolution has to be based on the adjustment of the bond angles [50–55], since the individual nearest-neighbor bond distances, such as d_{Zn-S} and d_{Cd-S}, do not change appreciably from their values in the end members (see Fig. 5), but the second nearest-neighbor distances, determined by the nearest-neighbor bond distances and the bond angles, change significantly. The second near-neighbor environment being a substituted cationic sublattice occuring farther away from the absorber atom, there is a larger spread in bond distances. Consequently, the σ^2 values, dominated mostly by static distortions, increase considerably (Supplemental Material Table S2 [70]) for any given composition, signifying the presence of a wide range of bond distances.

The knowledge of the nearest- and the next-nearest-neighbor distances from our EXAFS analysis allows us to estimate the average bond angles for Zn-S-Zn, Zn-S-Cd, and Cd-S-Cd following simple geometrical arguments; in Fig. 8(a), we have plotted these three bond angles obtained from the EXAFS analysis with solid symbols: circles, squares, and up-triangles, respectively. The corresponding values obtained from calculations are shown by corresponding open symbols in Fig. 8(b), establishing a good agreement between experiment and theory. The dashed, horizontal lines in Figs. 8(a) and 8(b) mark the ideal tetrahedral bond angle of 109.47°, which is found for the *M*-S-*M* angle with M = Zn or Cd for the end members. The range of the *M*-S-*M* angles were

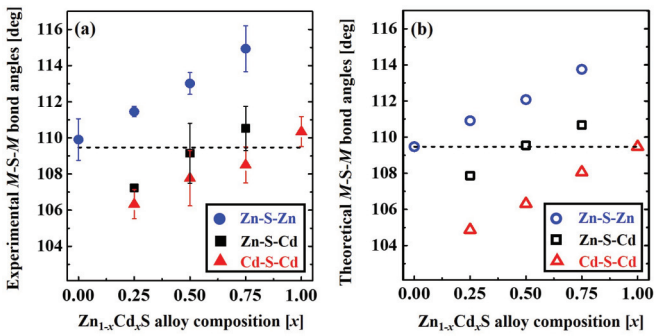

FIG. 8. (Color online) *M*-S-*M* (M = Zn or Cd or both) bond angles in the second near-neighbor environment for $Zn_{1-x}Cd_xS$ alloys obtained from (a) experiment and (b) theory. Zn-S-Zn (solid blue circles), Zn-S-Cd (solid black squares), and Cd-S-Cd (solid red up-triangles) bond angles are shown for the second shell as extracted from EXAFS; the theoretically calculated values from geometry optimization procedure are shown with corresponding open symbols. The horizontal, black dashed line represents the ideal tetrahedral bond angle (109.47°). Error limits for the theoretical data points, being smaller than the symbol size, have been removed.

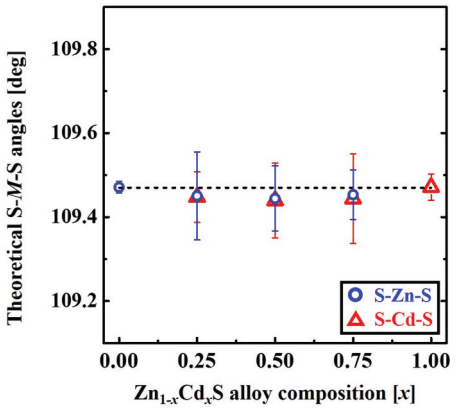

FIG. 9. (Color online) S-M-S bond angles for $Zn_{1-x}Cd_xS$ alloys obtained from theoretical calculations. We note that both S-Zn-S (open blue circles) and S-Cd-S (solid red up-triangles) angles assume the ideal tetrahedral bond angle value of 109.47° (dashed, horizontal line), regardless of the alloy composition.

calculated using the σ values for the respective M-S and M-M pairs. Clearly, the bond angles corresponding to Zn-S-Zn and Cd-S-Cd progressively deviate from the ideal tetrahedral angle with an increasing presence of the other cation, namely Cd and Zn, respectively. Specifically, the Zn-S-Zn angle increases with an increasing doping of Cd in ZnS; this can be understood as a consequence of accommodating larger sized Cd ions in the lattice. Exactly the reverse happens with the Cd-S-Cd angle with doping the smaller sized Zn ions in the CdS lattice.

Taking note of the quantitative agreement between the experimental and the calculated results for Zn-S-Zn, Zn-S-Cd, and Cd-S-Cd angles in Figs. 8(a) and 8(b), we make use of the theoretical data to understand the evolution of the S-Cd-S and S-Zn-S angles in absence of experimental EXAFS data at the S-edge. Interestingly, unlike the M-S-M angles in Fig. 8, both S-Zn-S and S-Cd-S angles, shown in Fig. 9, remain close to the ideal values of the end members. This observation at once provides us with a physical picture to understand how the local structure evolves into the global structure in such a cationic substituted solid solution. Combining with the near invariance of the Zn-S and Cd-S bond lengths in Figs. 5(a) and 5(b), Fig. 9 establishes Zn-S_4 and Cd-S_4 as fundamental, relatively rigid units that act as the building blocks of the solid solution, with these tetrahedral units rotating with respect to each other (see Fig. 8). These rotations of the M-S_4 tetrahedra with respect to each other are responsible for the progressive increase of Zn-S-Zn angle, ensuring that the next-near-neighbor Zn-Zn distance increases more rapidly than would be anticipated on the basis of relative invariance of the nearest neighbor Zn-S distance. It also ensures a decrease of the Cd-S-Cd angle with an increasing Zn composition of the alloy, likewise allowing for a more rapid variation of the next-near-neighbor Cd-Cd distance. Thus, the relatively rigid rotations of the M-S_4 tetrahedral units constitute the underlying microscopic mechanism by which the local, short length-scale structure, relatively invariant of the alloy composition, evolves into the global, long length-scale structure that follows the composition almost linearly across the solid solution conforming to Vegard's law. In order to ascertain the length scale of this phenomenon, we have probed the farther distances involved in the third coordination shell.

C. Third shell environment

The third shell of a cation, Zn or Cd, consists uniquely of S ions, as in the first shell. This farther away S shell, being quite far away from the absorbing atom, leads to a poor signal-to-noise ratio for EXAFS and has, therefore, rarely been investigated for such compounds. The experimental results for the third coordination shell obtained from the EXAFS analysis are presented in Fig. 10 as a function of the composition. The details of the local parameters extracted from the analyses are provided in Supplemental Material Table S3 [70]. The two sets of Zn-S distances are shown with solid black squares (short distance Zn-S1, degeneracy = 1) and solid blue circles (long distance Zn-S2, degeneracy = 9), whereas the two sets of Cd-S distances are shown in solid wine-colored down-triangles (short distance Cd-S1, degeneracy = 1) and solid red up-triangles (long distance Cd-S2, degeneracy = 9) in Fig. 10(a). The corresponding average theoretical values are shown with open symbols in Fig. 10(b), showing a good agreement in every case. The dashed line in the same figure represents the hypothetical single "average cation"-sulfur distance in the VCA sense with a degeneracy of nine, as explained in the Experimental Details section that tracks the composition-weighted average of the cation-sulfur distance of the end members. The dotted line represents the corresponding shorter M-S1 "average cation"-sulfur distance with degeneracy = 1. Clearly, the Zn-S and Cd-S in the third nearest-neighbor positions are close to this virtual crystal line,

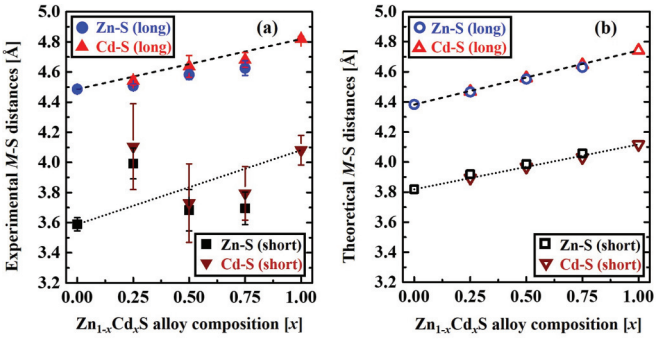

FIG. 10. (Color online) Third coordination shell interatomic distances for $Zn_{1-x}Cd_xS$ alloys obtained from (a) experiment and (b) theory. The experimental results are shown with solid black squares (short distance, degeneracy = 1), solid blue circles (long distance, degeneracy = 9) for Zn-S, solid wine-colored down-triangles (short distance, degeneracy = 1), and solid red up-triangles (long distance, degeneracy = 9) for Cd-S, whereas the theoretical values obtained from geometry optimization procedure are shown with corresponding open symbols. The black dotted and dashed lines connecting the two M-S (M = Zn or Cd) interatomic distances with degeneracies 1 and 9 of the pure end compounds schematically show the nature of a hypothetical average M-S bond length across the series, respectively, for both experiment and theory. Error limits for the theoretical data points, being smaller than the symbol size, have been removed. A comparison of (a) and (b) shows that their trends are very similar, as obtained from the slope of lines joining the individual data points.

the deviations in the rate of change of interatomic distances in terms of corresponding η being (45 ± 8)% and (3 ± 14)% for the Zn-S and Cd-S, respectively. These values, when compared to the deviations of (89 ± 4)% and (87 ± 5)% for the nearest-neighbor Zn-S and Cd-S distances discussed before (Fig. 5), clearly establish the rapid progress of the local structure obtained from the EXAFS data to the global structure deduced from XRD and the linear variation of the lattice parameters on the composition. Thus, the local distortions caused by ionic substitution are accommodated by an interplay between some relatively minor changes in the interatomic distances and requisite changes in bond angles in order to accommodate substitution of dissimilarly sized cations into the lattice. The rapid evolution of the local structure toward the global structure within a short length scale is crucial in preserving the well-defined unit cell lattice parameters, resulting in sharp diffraction patterns in such disordered alloy systems. We note that the percentage deviation for the Zn-S atom pair correlation for the third shell is still high, being almost close to the atom pair correlations of the second shell, the reason of which is not very clear to us as of now. We are performing calculations on a much larger supercell to understand the same. It is interesting to note that the nearest-neighbor Zn-S and Cd-S distances are completely distinct, making it impossible to attempt a description of its structural evolution in an average sense (Fig. 5); however, in contrast, the third nearest-neighbor Zn-S and Cd-S bond distances (shown in Fig. 10) are quite similar for any given composition.

Thus, a coarse-grained description of the alloy structure over length scales larger than the third nearest-neighbor distance may indeed be sufficiently captured within a VCA-type approach.

IV. SUMMARY

In order to summarize our most important findings, we first note that for any given atom pair, such as Zn-S or Cd-S in the nearest- or the third nearest-neighbor positions or Zn-Zn, Zn-Cd, or Cd-Cd in the second nearest-neighbor positions, an argument based on the VCA or motivated by the linear variation of the lattice parameters in accordance with Vegard's law would allow one to anticipate a linear dependence with the composition, characterized by the slope of the dashed line in Figs. 5, 7, and 10. In reality, we have shown that all these distances, though roughly changing linearly with the composition, have very different slopes than that of the dashed line given by Vegard's law. In Fig. 11, we plot the percentage deviation of slope found from EXAFS analysis ($m_{\text{expt.}}$) for each atom pair from the idealized slope (m_{VCA}) of the dashed line as a function of the average distance of that of the specific atom pair. This plot clearly shows how, at shorter distances, there is a strong deviation from the expectation based on simplified VCA-type arguments, while at longer distances such an approximate description becomes increasingly suitable. Combining our experimental results at the cationic K edges with our theoretical results, also available for the anionic sublattice, we provide a simple physical way to understand the crystal structure of the solid solutions. We find that the M-S_4 (M = Zn and Cd) units are only slightly affected across the series, retaining their tetrahedral integrity, and the

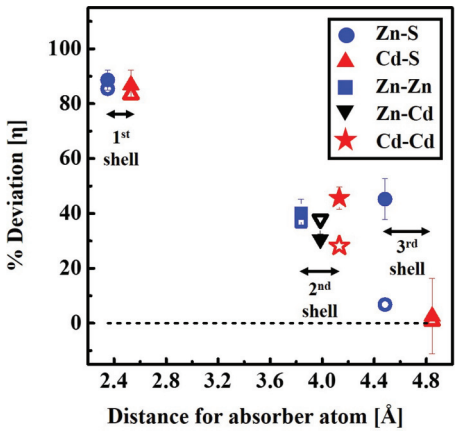

FIG. 11. (Color online) Systematic decrease of percentage deviation (η) defined as $(m_{\text{VCA}} - m_{\text{expt.}})/m_{\text{VCA}} \times 100$ for different shells in $Zn_{1-x}Cd_xS$ alloys with increasing distance from the absorber atom. The specific atom pairs obtained from experimental results are depicted in different closed symbols in the text box. The corresponding values obtained from theoretical calculations are shown in open symbols. The horizontal double arrows signify the spread of the interatomic distances within a particular coordination shell, which systematically increase with increasing distance from an absorber Zn and Cd. We can clearly see how rapidly the local structure evolves with interatomic distances to merge with the global description eventually. The black dashed, horizontal line represents the "zero-deviation" limit where the local structure matches with the global structure. Error limits for the theoretical data points, being smaller than the symbol size, have been removed.

dominant part of the evolution of the crystal parameters across the solution is achieved by a relative tilting of the different M-S_4 tetrahedral units against each other.

Figure 11 allows us to relate the actual microscopic changes in the atomic positions at various length scales to the concept of the chemical pressure that has been used extensively in the literature to tune properties of a range of materials [76,77]. The origin of this concept indeed lies in the observation that the doping of a smaller ion (typically with the same ionic state to avoid any charge doping) decreases the overall lattice parameter of the sample, similar to what can be achieved by applying an external hydrostatic pressure on the sample. Thus, the effect of doping a smaller ion has been considered equivalent to an external compressive stress of the sample. Based on the scaling of bond lengths with the lattice parameters on the application of an external hydrostatic pressure, it has been expected on the basis of the presumed equivalence between the hydrostatic pressure and doping that bond lengths would change following the change in the lattice parameters on doping too. However, our results here clearly show that the nearest-neighbor bond lengths do not scale with the lattice parameter change, showing a deviation as high as (89 ± 4)% (for Zn-S) and (87 ± 5)% (for Cd-S) from the lattice parameter variation on doping. Since hopping matrix elements, which dominate the electronic and magnetic structures of most interesting materials, is dominated by the nearest-neighbor contribution, falling off rapidly with distance, it is clear that the effect of doping on physical properties via the change in the bond distances

will be much smaller than that would be anticipated by the corresponding changes in the lattice parameter. This is in sharp contrast with the influence physical pressure would have on properties of any material, as bond distances, and specifically the nearest-neighbor ones, roughly follow the rate of change of lattice parameters in most cases. The case of the so-called "chemical pressure" is further complicated by the change in the angles between the M-S_4 tetrahedral units (Fig. 8) that are necessarily present to accommodate the changes in the lattice parameters in relative absence of corresponding changes in the nearest-neighbor distances (Fig. 5). It is well known that physical properties of a solid material are strongly influenced by such metal-ligand-metal bond angles in conjunction with the nearest-neighbor metal-ligand distances, as these two dictate the band formation in the solid. The variations in the bond angle and the nearest-neighbor bond distance may even oppose each other. Such complexities and much subdued percentage variations in the bond lengths compared to that in the lattice parameters on doping establish that the notion of a chemical pressure being analogous to the physical pressure may have to be abandoned, or at least used with great care.

ACKNOWLEDGMENTS

We thank Department of Science and Technology (DST), Council of Scientific and Industrial Research (CSIR), National Science Foundation (NSF), and Deutsche Forschungsgemeinschaft (DFG) for funding this investigation. X-ray Science Division partnered with the Pacific Northwest Consortium (PNC/XSD) facilities at the Advanced Photon Source, and research at these facilities, are supported by the US Department of Energy (DOE)—Basic Energy Sciences, a Major Resources Support grant from The Natural Sciences and Engineering Research Council of Canada (NSERC), the University of Washington, the Canadian Light Source and the Advanced Photon Source. Use of the Advanced Photon Source, an Office of Science User Facility operated for the DOE Office of Science by Argonne National Laboratory, was supported by the DOE under Contract No. DE-AC02-06CH11357. Support from the Swedish Research Council (VR), the KAW foundation, STANDUPP, eSSENCE and the ERC (ASD—Project No. 247062) is also acknowledged. Support for CUS was provided in part by the National Science Foundation under Grant No. DMR-086935.

[1] R. E. Nahory, M. A. Pollack, W. D. Johnston, Jr., and R. L. Barns, Appl. Phys. Lett. **33**, 659 (1978).
[2] J. C. Mikkelsen, Jr. and J. B. Boyce, Phys. Rev. B **28**, 7130 (1983).
[3] A. Balzarotti, N. Motta, A. Kisiel, M. Zimnal-Starnawska, M. T. Czyznyk, and M. Podgórny, Phys. Rev. B **31**, 7526 (1985).
[4] Z. Wu, K. Lu, Y. Wang, J. Dong, H. Li, C. Li, and Z. Fang, Phys. Rev. B **48**, 8694 (1993).
[5] J. Pellicer-Porres, A. Polian, A. Segura, V. Muñoz-Sanjosé, A. Di Cicco, and A. Traverse, J. Appl. Phys. **96**, 1491 (2004).
[6] E. Sidot, A. Kahn-Harari, E. Cesari, and L. Robbiola, Mater. Sci. Eng. A **393**, 147 (2005).
[7] H. L. Ray, N. Zhao, and L. C. De Jonghe, Electrochim. Acta **78**, 294 (2012).
[8] J. Fritsch, O. F. Sankey, K. E. Schmidt, and J. B. Page, J. Phys.: Condens. Matter **11**, 2351 (1999).
[9] L. Vegard, Z. Phys. **5**, 17 (1921).
[10] A. R. Denton and N. W. Ashcroft, Phys. Rev. A **43**, 3161 (1991).
[11] R. J. Heritage, P. Porteous, and B. J. Sheppard, J. Mater. Sci. **5**, 709 (1970).
[12] N. Nishiyama, J. Lin, A. Okazaki, M. Iwasaka, and K. Hirakawa, Jpn. J. Appl. Phys. **29**, 369 (1990).
[13] M. J. Lambregts and S. Frank, Talanta **62**, 627 (2004).
[14] M. Castellanos and A. R. West, J. C. S. Faraday I **76**, 2159 (1980).
[15] P. Ganguly, N. Shah, M. Phadke, V. Ramaswamy, and I. S. Mulla, Phys. Rev. B **47**, 991 (1993).
[16] W. Li, M. Pessa, and J. Likonen, Appl. Phys. Lett. **78**, 2864 (2001).
[17] D. Zhou and B. F. Usher, J. Phys. D: Appl. Phys. **34**, 1461 (2001).
[18] C. Bocchi, S. Franchi, F. Germini, A. Baraldi, R. Magnanini, D. De Salvador, M. Berti, and A. V. Drigo, J. Appl. Phys. **89**, 4676 (2001).
[19] A. V. G. Chizmeshya, M. R. Bauer, and J. Kouvetakis, Chem. Mater. **15**, 2511 (2003).
[20] Y. Kuo, B. Liou, S. Yen, and H. Chu, Opt. Commun. **237**, 363 (2004).
[21] B. Liou, S. Yen, and Y. Kuo, Appl. Phys. A **81**, 651 (2005).
[22] S. T. Murphy, A. Chroneos, C. Jiang, U. Schwingenschlögl, and R. W. Grimes, Phys. Rev. B **82**, 073201 (2010).
[23] V. S. Usurov, J. Str. Chem. **33**, 68 (1992).
[24] K. A. Gschneidner and G. H. Vineyard, J. Appl. Phys. **33**, 3444 (1962).
[25] M. Park, T. E. Mitchell, and A. H. Heuer, J. Am. Ceram. Soc. **58**, 43 (1975).
[26] J. Friedel, Phil. Mag. **46**, 514 (1955).
[27] H. E. Steinwehr, Z. Krist. **125**, 360 (1967).
[28] K. T. Jacob, S. Raj, and L. Rannesh, Int. J. Mater. Res. **98**, 776 (2007).
[29] A. A. R. Fernandes, J. Santamaria, S. L. Bud'ko, O. Nakamura, J. Guimpel, and I. K. Schuller, Phys. Rev. B **44**, 7601 (1991).
[30] H. C. Nguyen and J. B. Goodenough, Phys. Rev. B **52**, 324 (1995).
[31] Y. Moritomo, H. Kuwahara, Y. Tomioka, and Y. Tokura, Phys. Rev. B **55**, 7549 (1997).
[32] F. Licci, A. Gauzzi, M. Marezio, G. P. Radaelli, R. Masini, and C. Chaillout-Bougerol, Phys. Rev. B **58**, 15208 (1998).
[33] M. Kriener, C. Zobel, A. Reichl, J. Baier, M. Cwik, K. Berggold, H. Kierspel, O. Zabara, A. Freimuth, and T. Lorenz, Phys. Rev. B **69**, 094417 (2004).
[34] J. Azoulay, E. A. Stern, D. Shaltiel, and A. Grayevski, Phys. Rev. B **25**, 5627 (1982).
[35] J. C. Mikkelsen, Jr. and J. B. Boyce, Phys. Rev. Lett. **49**, 1412 (1982).
[36] A. Balzarotti, M. Czyznyk, A. Kisiel, N. Motta, M. Podgòrny, and M. Zimnal-Starnawska, Phys. Rev. B **30**, 2295(R) (1984).
[37] A. Bunker, J. Vac. Sci. Technol. A **5**, 3003 (1987).

[38] R. A. Mayanovic, W.-F. Pong, and B. A. Bunker, Phys. Rev. B **42**, 11174 (1990).
[39] S. M. Islam and B. A. Bunker, Phys. Lett. A **156**, 247 (1991).
[40] A. Kisiel, J. Lazewski, M. Zimnal-Starnawska, E. Burattini, and A. Mycielski, J. Phys. IV France **7**, C2-1197 (1997).
[41] R. J. Iwanowski, K. Ławniczak-Jablońska, I. Winter, and J. Hormes, Solid State Commun. **97**, 879 (1996).
[42] Q. Lu, B. A. Bunker, H. Luo, A. J. Kropf, K. M. Kemner, and J. K. Furdyna, Phys. Rev. B **55**, 9910 (1997).
[43] J. B. Boyce and J. C. Mikkelsen, Jr., Phys. Rev. B **31**, 6903 (1985).
[44] N. Motta, A. Balzarotti, P. Letardi, A. Kisiel, M. T. Czyżyk, M. Zimnal-Starnawska, and M. Podgórny, Solid State Commun. **53**, 509 (1985).
[45] J. B. Boyce and J. C. Mikkelsen, Jr., J. Cryst. Growth **98**, 37 (1989).
[46] S. Pascarelli, F. Boscherini, S. Mobilio, K. Lawniczak-Jablonska, and R. Kozubski, Phys. Rev. B **49**, 14984 (1994).
[47] J. Łażewski, M. Zimnal-Starnawska, A. Kisiel, F. Boscherini, S. Pascarelli, and W. Giriat, Phys. Status Solidi B **197**, 7 (1996).
[48] A. I. Frenkel, V. Sh. Machavariani, A. Rubshtein, Yu. Rosenberg, A. Voronel, and E. A. Stern, Phys. Rev. B **62**, 9364 (2000).
[49] I. Yonenaga and M. Sakurai, Phys. Rev. B **64**, 113206 (2001).
[50] W.-F. Pong, R. A. Mayanovic, B. A. Bunker, J. K. Furdyna, and U. Debska, Phys. Rev. B **41**, 8440 (1990).
[51] A. Frenkel, E. A. Stern, A. Voronel, M. Qian, and M. Newville, Phys. Rev. Lett. **71**, 3485 (1993).
[52] A. Frenkel, A. Voronel, A. Katzir, M. Newville, and E. A. Stern, Physica B **208-209**, 334 (1995).
[53] A. I. Frenkel, E. A. Stern, A. Voronel, and S. M. Heald, Solid State Commun. **99**, 67 (1996).
[54] N. Happo, H. Sato, T. Mihara, S. Hosokawa, Y. Ueda, and M. Taniguchi, J. Phys.: Condens. Matter **8**, 4315 (1996).
[55] T. Ganguli, J. Mazher, A. Polian, S. K. Deb, F. Villain, O. Pages, W. Paszkowicz, and F. Firszt, J. App. Phys. **108**, 083539 (2010).
[56] B. V. Robouch and A. Kisiel, J. Alloys Compd. **286**, 80 (1996).
[57] M. E. Rincón, M. W. Martínez, and M. Miranda-Hernández, Thin Solid Films **425**, 127 (2003).
[58] C. Xing, Y. Zhang, W. Yan, and L. Guo, Int. J. Hydrogen Energy **31**, 2018 (2006).
[59] Y. Hsu, S. Lu, and Y. Lin, Adv. Funct. Mater. **15**, 1350 (2005).
[60] Y. Liu, J. A. Zapien, Y. Y. Shan, C. Geng, C. S. Lee, and S. Lee, Adv. Funct. Mater. **17**, 1372 (2005).
[61] Y. Lin, Y. Hsu, S. Lu, K. Chen, and T. Tseng, J. Phys. Chem. C **111**, 13418 (2007).
[62] Y. Chen, X. Zhang, C. Jia, Y. Su, and Q. Li, J. Phys. Chem. C **113**, 2263 (2009).
[63] A. Nag, S. Chakraborty, and D. D. Sarma, J. Am. Chem. Soc. **130**, 10605 (2008).
[64] Z. Wang, P. B. Griffin, J. McVittie, S. Wong, P. C. McIntyre, and Y. Nishi, IEEE Electron Device Lett. **28**, 1 (2007).
[65] Y. S. Murty, B. S. Naidu, and P. J. Reddy, Mater. Sci. Eng. B **8**, 175 (1991).
[66] N. Roushdy, A. A. M. Farag, M. A. Rafea, O. El-Shazly, and E. F. El-Wahidy, Superlattices Microstruct. **62**, 97 (2013).
[67] S. B. Qadri, E. F. Skelton, D. Hsu, A. D. Dinsmore, J. Yang, H. F. Gray, and B. R. Ratna, Phys. Rev. B **60**, 9191 (1999).
[68] B. Ravel and M. Newville, J. Synch. Rad. **12**, 537 (2005).
[69] S. I. Zabinsky, J. J. Rehr, A. Ankudinov, R. C. Albers, and M. J. Eller, Phys. Rev. B **52**, 2995 (1995).
[70] See Supplemental Material at http://link.aps.org/supplemental/10.1103/PhysRevB.89.224105 for details of EXAFS data analysis.
[71] J. M. Soler, E. Artacho, J. D. Gale, A. Garcia, J. Junquera, P. Ordejón, and D. Sánchez-Portal, J. Phys.: Condens. Matter **14**, 2745 (2002).
[72] J. P. Perdew and A. Zunger, Phys. Rev. B **23**, 5048 (1981).
[73] F. Tran, R. Laskowski, P. Blaha, and K. Schwarz, Phys. Rev. B **75**, 115131 (2007).
[74] H. C. Weissker, J. Furthmuller, and F. Bechstedt, Phys. Rev. B **67**, 245304 (2003).
[75] C. Meneghini, S. Ray, F. Liscio, F. Bardelli, S. Mobilio, and D. D. Sarma, Phys. Rev. Lett. **103**, 046403 (2009).
[76] H. Nakamura, H. Wada, K. Yoshimura, M. Shiga, Y. Nakamura, J. Sakurai, and Y. Komura, J. Phys. F: Met. Phys. **18**, 981 (1988).
[77] Y. Moritomo, Sh. Xu, A. Machida, T. Katsufuji, E. Nishibori, M. Takata, M. Sakata and S-W. Cheong, Phys. Rev. B **63**, 144425 (2001).